

## Thickness-Independent Capacitive Performance of Holey $Ti_3C_2T_x$ Film Prepared through a Mild Oxidation Strategy

Guo, Rui; Yuan, Peng; Han, Xiyang; He, Xuexia; Lu, Jiangbo; Li, Qi; Dang, Liqin; Sun, Jie; Liu, Zonghuai; Lei, Zhibin

**DOI**

[10.1002/smll.202205947](https://doi.org/10.1002/smll.202205947)

**Publication date**

2022

**Document Version**

Final published version

**Published in**

Small

**Citation (APA)**

Guo, R., Yuan, P., Han, X., He, X., Lu, J., Li, Q., Dang, L., Sun, J., Liu, Z., & Lei, Z. (2022). Thickness-Independent Capacitive Performance of Holey  $Ti_3C_2T_x$  Film Prepared through a Mild Oxidation Strategy. *Small*, 19(9), Article 2205947. <https://doi.org/10.1002/smll.202205947>

**Important note**

To cite this publication, please use the final published version (if applicable).  
Please check the document version above.

**Copyright**

Other than for strictly personal use, it is not permitted to download, forward or distribute the text or part of it, without the consent of the author(s) and/or copyright holder(s), unless the work is under an open content license such as Creative Commons.

**Takedown policy**

Please contact us and provide details if you believe this document breaches copyrights.  
We will remove access to the work immediately and investigate your claim.

# Thickness-Independent Capacitive Performance of Holey $\text{Ti}_3\text{C}_2\text{T}_x$ Film Prepared through a Mild Oxidation Strategy

Rui Guo, Peng Yuan, Xiying Han, Xuexia He, Jiangbo Lu, Qi Li, Liqin Dang, Jie Sun, Zonghuai Liu, and Zhibin Lei\*

The  $\text{Ti}_3\text{C}_2\text{T}_x$  film with metallic conductivity and high pseudo-capacitance holds profound promise in flexible high-rate supercapacitors. However, the restacking of  $\text{Ti}_3\text{C}_2\text{T}_x$  sheets hinders ion access to thick film electrodes. Herein, a mild yet green route has been developed to partially oxidize  $\text{Ti}_3\text{C}_2\text{T}_x$  to  $\text{TiO}_2/\text{Ti}_3\text{C}_2\text{T}_x$  by introducing  $\text{O}_2$  molecules during refluxing the  $\text{Ti}_3\text{C}_2\text{T}_x$  suspension. The subsequent etching away of these  $\text{TiO}_2$  nanoparticles by HF leaves behind numerous in-plane nanopores on the  $\text{Ti}_3\text{C}_2\text{T}_x$  sheets. Electrochemical impedance spectroscopy shows that longer oxidation time of 40 min yields holey  $\text{Ti}_3\text{C}_2\text{T}_x$  (H- $\text{Ti}_3\text{C}_2\text{T}_x$ ) with a much shorter relax time constant of 0.85 s at electrode thickness of 25  $\mu\text{m}$ , which is 89 times smaller than that of the pristine  $\text{Ti}_3\text{C}_2\text{T}_x$  film (75.58 s). Meanwhile, H- $\text{Ti}_3\text{C}_2\text{T}_x$  film with 25 min oxidation exhibits less-dependent capacitive performance in film thickness range of 10–84  $\mu\text{m}$  (1.63–6.41  $\text{mg cm}^{-2}$ ) and maintains around 60% capacitance as the current density increases from 1 to 50  $\text{A g}^{-1}$ . The findings clearly demonstrate that in-plane nanopores not only provide more electrochemically active sites, but also offer numerous pathways for rapid ion impregnation across the thick  $\text{Ti}_3\text{C}_2\text{T}_x$  film. The method reported herein would pave way for fabricating porous MXene materials toward high-rate flexible supercapacitor applications.

## 1. Introduction

Supercapacitors are regarded as promising energy storage devices with unique features including rapid charge-discharge rate, high power density, and ultralong cycle life.<sup>[1–3]</sup> In

R. Guo, P. Yuan, X. Han, X. He, Q. Li, L. Dang, J. Sun, Z. Liu, Z. Lei  
Key Laboratory of Applied Surface and Colloid Chemistry  
MOE

Shaanxi Engineering Lab for Advanced Energy Technology  
Shaanxi Key Laboratory for Advanced Energy Devices  
School of Materials Science and Engineering  
Shaanxi Normal University  
620 West Chang'an Street, Xi'an, Shaanxi 710119, China  
E-mail: zblei@snnu.edu.cn

R. Guo  
Department of Radiation Science and Technology  
Faculty of Applied Sciences  
Delft University of Technology  
Mekelweg 15, Delft 2629JB, The Netherlands

J. Lu  
School of Physics & Information Technology  
Shaanxi Normal University  
620 West Chang'an Street, Xi'an, Shaanxi 710119, China

 The ORCID identification number(s) for the author(s) of this article can be found under <https://doi.org/10.1002/smll.202205947>.

DOI: 10.1002/smll.202205947

particular, substantial efforts have been devoted to design flexible, lightweight, and ultra-stable supercapacitors to meet the fast growing demand of diverse wearable and portable electronic devices.<sup>[4–7]</sup> According to the charge storage mechanism, supercapacitors can be classified into electric double layer capacitors (EDLCs) based on the fast ion adsorption at the electrode/electrolyte interfaces and the pseudocapacitors via surface Faraday redox reactions.<sup>[8,9]</sup> The specific capacitances of EDLC electrodes such as graphene,<sup>[10]</sup> carbon nanotubes,<sup>[11]</sup> and biomass-derived carbon materials<sup>[12,13]</sup> are usually around 200  $\text{F g}^{-1}$  due to their limited specific surface area. In contrast, the pseudocapacitive materials such as  $\text{MnO}_2$ ,<sup>[14]</sup>  $\text{Fe}_2\text{O}_3$ ,<sup>[15]</sup> and NiCo LDH<sup>[16]</sup> exhibit significantly high specific capacitance. However, because of their poor electrical conductivity and unsatisfying electrochemical stability, they are usually hybridized with other highly conductive substrates such as carbon materials<sup>[17]</sup> and metal foil substrates<sup>[18]</sup> to enhance the conductivity. These conductive substrates with large weight but contributes negligible capacitance.

MXenes, 2D transition metal carbides, nitrides, or carbonitrides, have been intensively studied and show competitive performances in various fields including energy storage,<sup>[19–21]</sup> catalysis,<sup>[22,23]</sup> environmental and water treatment,<sup>[24,25]</sup> sensors,<sup>[26,27]</sup> and biomedical applications.<sup>[28,29]</sup> MXenes have general formula of  $\text{M}_{n+1}\text{X}_n\text{T}_x$  ( $n = 1–4$ ), where M represents the transition metal including Ti, V, Nb, Mo, and Cr, X stands for carbon and/or nitrogen, and  $\text{T}_x$  means the surface functional terminals (such as  $-\text{OH}$ ,  $-\text{O}$ ,  $-\text{Cl}$ , and  $-\text{F}$ ).<sup>[30,31]</sup> Among them, the first reported  $\text{Ti}_3\text{C}_2\text{T}_x$ <sup>[32]</sup> is most studied for supercapacitor application because of its intriguing physicochemical properties including high electrical conductivity, rich surface functional groups, high aspect ratio, and large proton-induced pseudocapacitance in acidic aqueous electrolytes.<sup>[33–35]</sup> Besides, another important nature of  $\text{Ti}_3\text{C}_2\text{T}_x$  is that it can be easily fabricated to a free-standing film by vacuum-assisted filtration technique. Although such film electrode does not involve the use of binders and conductive additives, those  $\text{Ti}_3\text{C}_2\text{T}_x$  sheets tend to restack due to the strong van der Waals forces between interlayers during the film fabrication process, leading to long ion transport pathway and less access of the electrolyte ions to

the active sites. This issue becomes more prominent with the increase of the film thickness.<sup>[36]</sup> Typical methods to alleviate the restacking of  $\text{Ti}_3\text{C}_2\text{T}_x$  sheets include the design of MXene to porous network structure through self-assembly strategy,<sup>[37,38]</sup> or introducing spacers between MXene sheets.<sup>[39,40]</sup> For example, Xu et al.<sup>[41]</sup> demonstrated the successful incorporation of CNTs to  $\text{Ti}_3\text{C}_2\text{T}_x$  film to increase the porosity and amount of inter-layer water. A specific capacitance of 375 and 251.2  $\text{F g}^{-1}$  for the hybrid electrode can be obtained at 5 and 1000  $\text{mV s}^{-1}$ , respectively. Liu et al.<sup>[42]</sup> prepared a flexible MXene/holey graphene film electrode with fast ion transport speed and short transport path. A symmetric supercapacitor built with this electrode delivered a fantastic volumetric energy density (38.6  $\text{Wh L}^{-1}$ ). Most recently, Gogotsi and his coworkers reported a  $\text{Ti}_3\text{C}_2/\text{PEDOT:PSS}$  hybrid electrode prepared by spray-coating method. The hybrid electrode is still capable of retaining 10.8% capacitance as the scan rate increased from 0.1 to 1000  $\text{V s}^{-1}$ , which proves such candidate to be a promising electrode for flexible AC-filtering electrochemical capacitor.<sup>[43]</sup> While insertion of nanomaterials and 3D-structure design enable easy access of electrolyte ions, the highly porous network would reduce the volumetric capacitance of the  $\text{Ti}_3\text{C}_2\text{T}_x$  electrodes due to the large number of macropores.

The creation of in-plane nanopores on  $\text{Ti}_3\text{C}_2\text{T}_x$  nanosheets allows fast ion penetration across the stacked holey film, which is beneficial to the volumetric capacitance. On the basis of the fact that  $\text{Ti}_3\text{C}_2\text{T}_x$  nanosheets are vulnerable to oxidation under humidity with high oxygen atmosphere, the in-plane nanopores can be facily generated by catalytic oxidization of  $\text{Ti}_3\text{C}_2\text{T}_x$  nanosheets with  $\text{Cu}^{2+}$  or through an in situ anodic oxidation strategy.<sup>[44,45]</sup> Despite that the improved rate performance can be achieved, such in situ electrochemical method is not applicable for large-scale fabrication. On the other hand, a controllable  $\text{H}_2\text{SO}_4$  oxidation method has also been developed to alleviate the restacking of  $\text{Ti}_3\text{C}_2\text{T}_x$  sheets, though the use of corrosive  $\text{H}_2\text{SO}_4$  may lead to other problems.<sup>[46]</sup> Therefore, the exploration of an effective solution to controllably fabricate holey  $\text{Ti}_3\text{C}_2\text{T}_x$  is of utmost importance for MXene-based energy storage materials.

Herein, we report a mild yet effective route to prepare holey  $\text{Ti}_3\text{C}_2\text{T}_x$  sheets ( $\text{H-Ti}_3\text{C}_2\text{T}_x$ ) by introducing  $\text{O}_2$  during the refluxing of  $\text{Ti}_3\text{C}_2\text{T}_x$  suspensions. The structure of  $\text{H-Ti}_3\text{C}_2\text{T}_x$  can be facily adjusted by controlling the reaction time. Longer oxidation duration yields  $\text{Ti}_3\text{C}_2\text{T}_x$  sheets with more in-plane nanopores. The electrochemical properties of the  $\text{H-Ti}_3\text{C}_2\text{T}_x$  films prepared at different oxidation durations ( $\text{H-Ti}_3\text{C}_2\text{T}_x\text{-}x$  with  $x$  representing the oxidation time in minutes) were systematically investigated. Moreover, the dependence of the electrode thickness and the electrochemical performance has also been investigated through electrochemical impedance spectroscopy (EIS). It is noticed that these in-plane nanopores can not only provide more electroactive sites for efficient charge storage, but can also significantly boost the ion impregnation across the dense  $\text{Ti}_3\text{C}_2\text{T}_x$  film. Correspondingly, higher specific capacitance, fast ion transport, and excellent rate capability can be achieved for the holey  $\text{H-Ti}_3\text{C}_2\text{T}_x$  film electrode. This controllable oxidation strategy is expected to offer a new avenue for the design of advanced MXene-based energy storage materials with different structures.

## 2. Results and Discussions

The  $\text{H-Ti}_3\text{C}_2\text{T}_x$  is derived from the selective removal of Ti atoms from pristine  $\text{Ti}_3\text{C}_2\text{T}_x$  nanosheets. First of all, the few-layer  $\text{Ti}_3\text{C}_2\text{T}_x$  nanosheets (Figure 1a) with clean surface and the lateral size of several micrometers were synthesized from  $\text{Ti}_3\text{AlC}_2$  precursor using the  $\text{LiF/HCl}$  mixture as the etchant.<sup>[47]</sup> The lateral size of the as synthesized  $\text{Ti}_3\text{C}_2\text{T}_x$  nanosheets is confirmed to be 1–3  $\mu\text{m}$  (Figure 1a) with the thickness of around 2 nm based on the results from atomic force microscopy analysis (Figure S1a, Supporting Information). The electrical conductivity of the  $\text{Ti}_3\text{C}_2\text{T}_x$  film with the thickness of 25  $\mu\text{m}$  can reach up to 4700  $\text{S cm}^{-1}$ , which is comparable to previous reported results.<sup>[48]</sup> After partial oxidation of the  $\text{Ti}_3\text{C}_2\text{T}_x$  nanosheets in a high-purity oxygen environment at 100  $^\circ\text{C}$ , the oxidized  $\text{Ti}_3\text{C}_2\text{T}_x$  nanosheets ( $\text{O-Ti}_3\text{C}_2\text{T}_x$ ) with clearly observed spherical and fusion particles are confirmed through transmission electron microscope (TEM) (Figure 1b). In addition, the size of these nanoparticles increases with the extending of oxidation time (Figure S2, Supporting Information). The line profile analysis along the yellow line in Figure S3, Supporting Information, presents two clear lattice fringes with the distance of 0.35 and 0.19 nm, corresponding to the (101) and (200) planes of anatase  $\text{TiO}_2$ , respectively (JCPDS no. 21-1272, Figure 1c,d).<sup>[49]</sup> The subsequent etching away of these  $\text{TiO}_2$  nanoparticles with HF leaves behind a large number of holes which are uniformly distributed on  $\text{Ti}_3\text{C}_2\text{T}_x$  sheets (Figure 1e–g). Obviously, the number of pores increases distinctly with the oxidation time, suggesting that the facile control of the pore density can be achieved by simply adjusting the oxidation time. In addition, a statistical analysis on over 200 pores reveals that the diameter of these in-plane nanopores varies from 2 to 10 nm with an average value of 4.5 nm (Figure 1i–k). The pore size is also confirmed to be less dependent on the oxidation time. Through the HRTEM image shown in Figure 1h, obvious amorphization can be found around the edge of pores, which is speculated as the leftover of carbon after the removal of Ti atoms by HF etching. It is worth mentioning that the 2D sheet-like structure and clean surface of  $\text{Ti}_3\text{C}_2\text{T}_x$  nanosheets are well maintained after etching away  $\text{TiO}_2$  particles from  $\text{O-Ti}_3\text{C}_2\text{T}_x$  nanosheets (Figure S4, Supporting Information).

To further illustrate the detailed structure around the holes on  $\text{H-Ti}_3\text{C}_2\text{T}_x$  nanosheets, the Cs-corrected scanning transmission electron microscopy (STEM) images have been collected, as shown in Figure 2a. It is noticed that  $\text{H-Ti}_3\text{C}_2\text{T}_x$  nanosheets exhibit excellent crystalline status under the observation direction along [0001] zone axis. Since the bright spots in the figure represent Ti atoms, the missing of some bright spots in the lattice can be considered as the vacancies left by the disappearance of Ti atoms after HF etching. Such phenomenon has also been confirmed in previous reports.<sup>[50]</sup> By constructing the fast Fourier transform (FFT) image, the typical diffraction spots of  $\text{Ti}_3\text{C}_2$  under [0001] zone axis can be indexed, as shown in Figure 2b,c. Moreover, the inverse fast Fourier transform (IFFT) image is also constructed to further illustrate the detailed structure at the edge of holes, as shown in Figure 2d. The lattice planes with the  $d$ -spacings of 0.15 and 0.27 nm have been marked in the figure, which correspond to (1 $\bar{1}$ 00) and (2 $\bar{1}$ 10) of  $\text{Ti}_3\text{C}_2$ , respectively. Seeing from the edge of the two

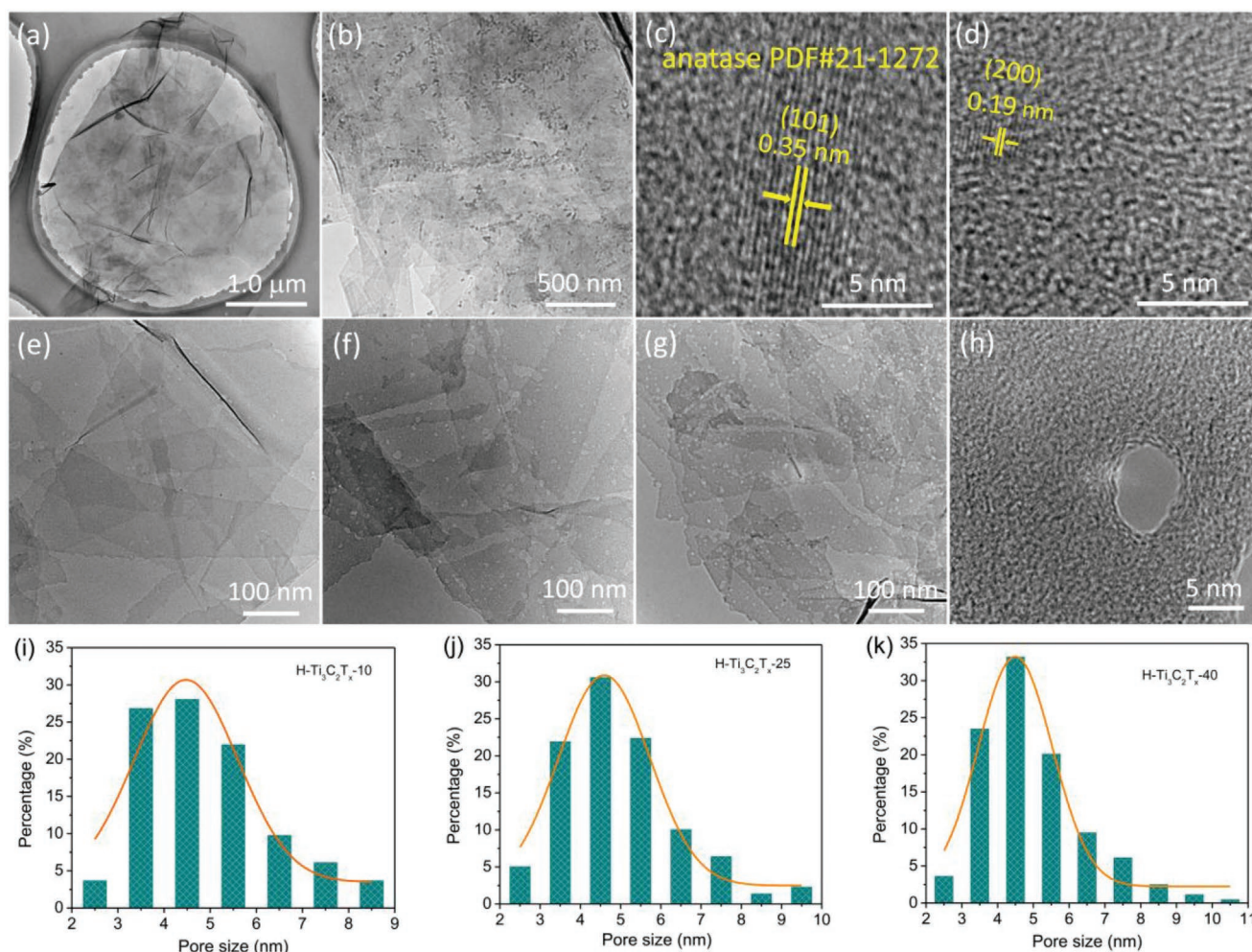


**Figure 1.** TEM images of the  $\text{Ti}_3\text{C}_2\text{T}_x$ -based nanosheets: a) pristine  $\text{Ti}_3\text{C}_2\text{T}_x$ , b–d)  $\text{O-Ti}_3\text{C}_2\text{T}_x$ -40, e)  $\text{H-Ti}_3\text{C}_2\text{T}_x$ -10, f)  $\text{H-Ti}_3\text{C}_2\text{T}_x$ -25, and g, h)  $\text{H-Ti}_3\text{C}_2\text{T}_x$ -40. i–k) Pore size statistical analysis of holey  $\text{Ti}_3\text{C}_2\text{T}_x$ .

holes in the figure, there is a transition region with the thickness of 0.5–2 nm at the edge, in which the crystal periodicity has been partially or completely destroyed. The displayed contrast may correspond to the remaining of carbon atoms after the etching away of Ti atoms. Similar phenomenon can also be seen for the hole edge in the integrated differential phase contrast (IDPC) STEM-BF image, which can display both light and heavy atoms at the same time, as illustrated in Figure 2e. As seen from the figure, the missing of some Ti atoms at the surface of  $\text{H-Ti}_3\text{C}_2\text{T}_x$  nanosheets is clearly visible, which is considered to generate after HF etching. The crystal model covered on the figure schematically illustrates the missing of specific atom columns. For the monolayer  $\text{Ti}_3\text{C}_2$ , when HF etches the Ti atoms on the surface of nanosheets, the remaining carbon atoms will accumulate due to the breakage of the Ti–C bond. Meanwhile, the highly active edge of the holes, which left after the etching away of  $\text{TiO}_2$  nanoparticles, becomes an ideal location for the accumulation of the above carbon atoms. This is the reason why carbon enrichment can be found around the etched holes at the surface of  $\text{Ti}_3\text{C}_2\text{T}_x$  nanosheets. Figure 2f schematically illustrate the as described formation process of the holes. The vacancies caused by HF etching will accumulate

together with the leftover C atoms (marked with red circles) at the edge until the final formation of holes.

The phase structures of  $\text{Ti}_3\text{C}_2\text{T}_x$  before and after the above oxidation process have also been characterized by XRD (Figure 3a). Compared with the (002) diffraction peaks of the pristine  $\text{Ti}_3\text{C}_2\text{T}_x$  film ( $6.26^\circ$ ), the peaks of all the  $\text{O-Ti}_3\text{C}_2\text{T}_x$  films slightly shift toward lower angle direction to  $2\theta = 6.17^\circ$ , suggesting the increased interlayer spacing of  $\text{O-Ti}_3\text{C}_2\text{T}_x$  nanosheets, which is considered to be the reason of the formation of  $\text{TiO}_2$  particles produced during the oxidation process (Figure 3b). Meanwhile, the intensity of the (002) diffraction peak for all  $\text{O-Ti}_3\text{C}_2\text{T}_x$  products also decreases gradually with the increase of oxidation time, suggesting the partial structure destruction of the  $\text{Ti}_3\text{C}_2\text{T}_x$  nanosheets after long time oxidation process. However, upon etching away the  $\text{TiO}_2$  particles between  $\text{Ti}_3\text{C}_2\text{T}_x$  layers by HF, the (002) peak of the  $\text{H-Ti}_3\text{C}_2\text{T}_x$  almost returns to the original position. It is worth to mention that the diffraction peaks of  $\text{TiO}_2$  were not observed in the  $\text{O-Ti}_3\text{C}_2\text{T}_x$  sample, which is presumably due to its low contents and poor crystalline process. Figure S5, Supporting Information, provides the X-ray photoelectron spectroscopy (XPS) survey spectra of pristine  $\text{Ti}_3\text{C}_2\text{T}_x$ ,  $\text{O-Ti}_3\text{C}_2\text{T}_x$ , and  $\text{H-Ti}_3\text{C}_2\text{T}_x$ .

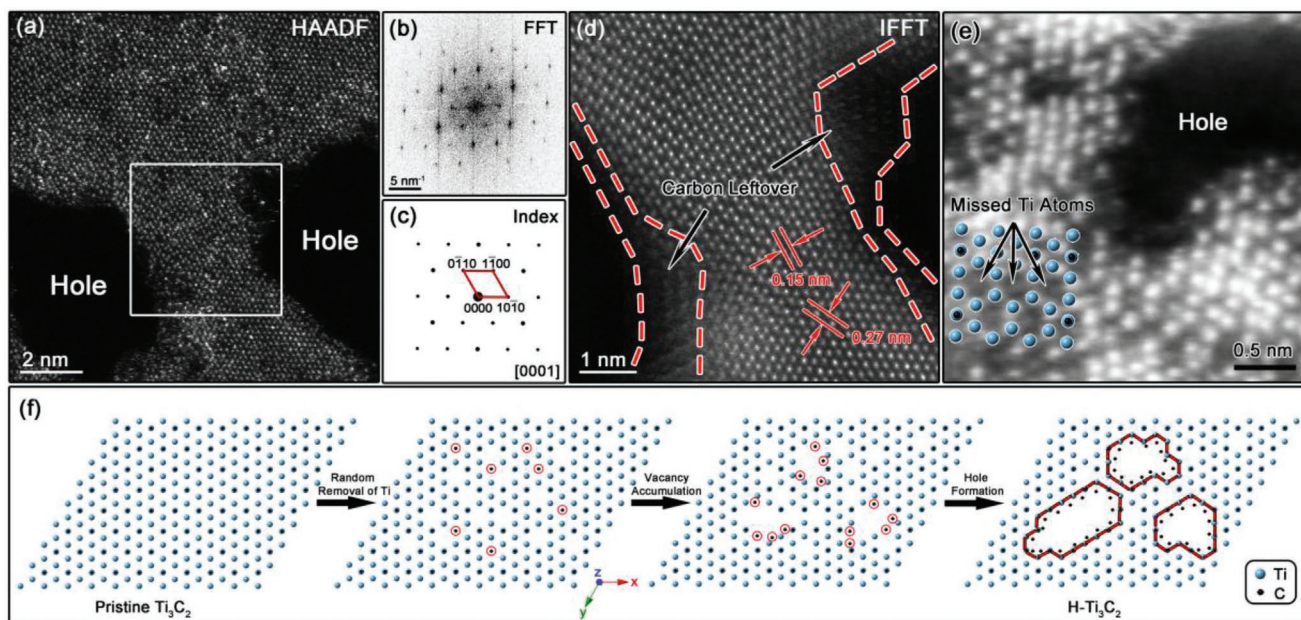


**Figure 2.** Cs-corrected STEM characterization results of H-Ti<sub>3</sub>C<sub>2</sub>T<sub>x</sub>-40 nanosheets: a) STEM-HAADF image, b) corresponding FFT figure, c) index of the FFT figure, d) enlarged IFFT image, e) IDPC STEM-BF image, and f) schematic formation process of the holes on Ti<sub>3</sub>C<sub>2</sub>T<sub>x</sub> nanosheets.

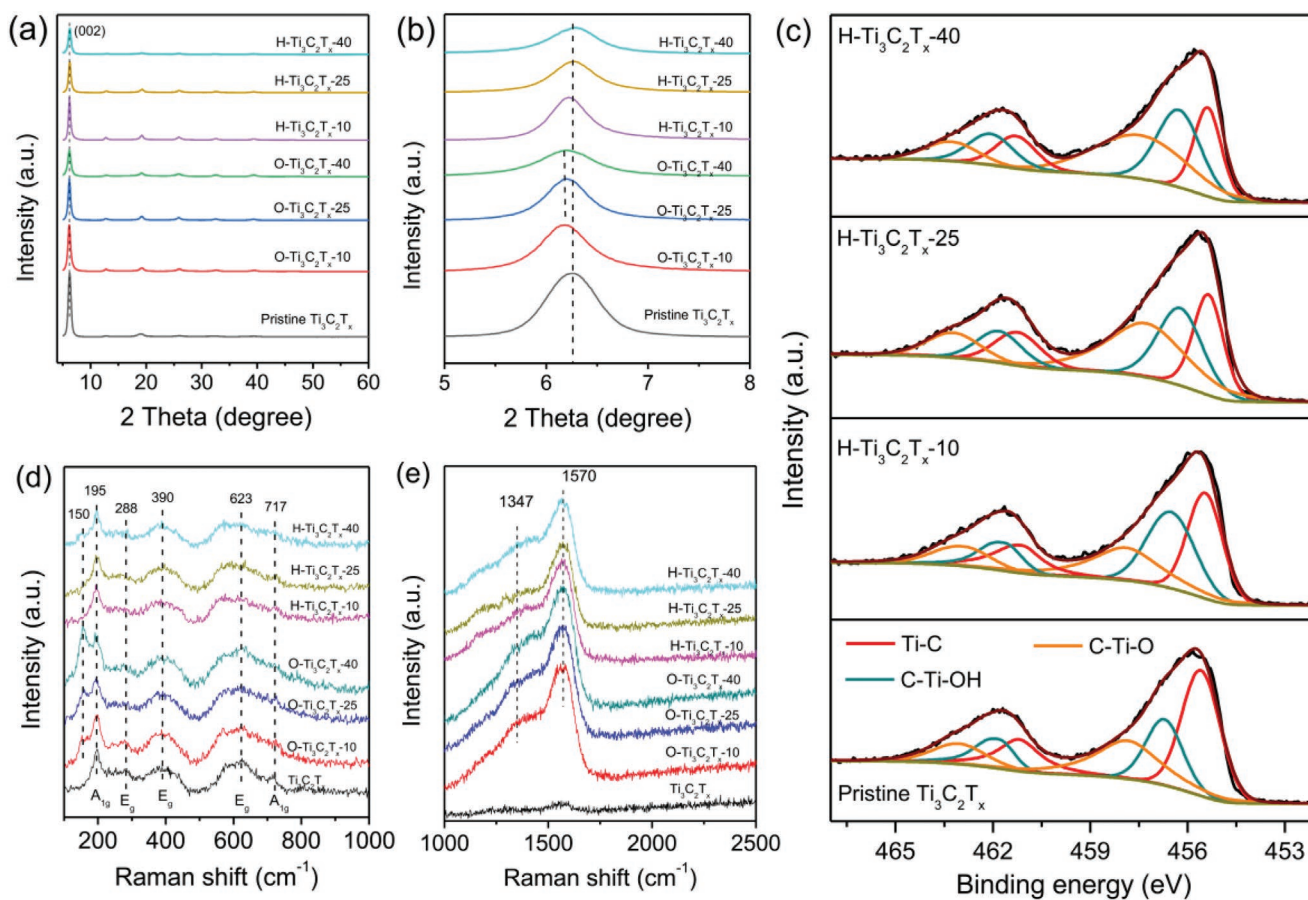


**Figure 3.** XRD, XPS, and Raman spectra characterization results of the pristine Ti<sub>3</sub>C<sub>2</sub>T<sub>x</sub> and H-Ti<sub>3</sub>C<sub>2</sub>T<sub>x</sub> films: a,b) XRD patterns of pristine Ti<sub>3</sub>C<sub>2</sub>T<sub>x</sub>, O-Ti<sub>3</sub>C<sub>2</sub>T<sub>x</sub>, and H-Ti<sub>3</sub>C<sub>2</sub>T<sub>x</sub> films, c) Ti 2p XPS spectra of pristine Ti<sub>3</sub>C<sub>2</sub>T<sub>x</sub> and H-Ti<sub>3</sub>C<sub>2</sub>T<sub>x</sub> films, and d,e) Raman spectra of pristine Ti<sub>3</sub>C<sub>2</sub>T<sub>x</sub>, O-Ti<sub>3</sub>C<sub>2</sub>T<sub>x</sub>, and H-Ti<sub>3</sub>C<sub>2</sub>T<sub>x</sub> films.

films, where the characteristic peaks of Ti, C, O, F, and Cl can be seen clearly. The Ti 2p XPS spectra of O-Ti<sub>3</sub>C<sub>2</sub>T<sub>x</sub> with different oxidation time are presented in Figure S6, Supporting Information. According to the quantitative analysis on Ti 2p core level spectra, a short time of 10 min oxidation leads to the formation of 7.26 at% TiO<sub>2</sub> in the whole peaks, which accounts for 1.43 at% in the resultant TiO<sub>2</sub>/O-Ti<sub>3</sub>C<sub>2</sub>T<sub>x</sub> composites (Table S1, Supporting Information). As the oxidation time prolongs to 40 min, the above value increase to 10.72 and 2.29 at%, respectively. This suggests that the surface oxidation of Ti<sub>3</sub>C<sub>2</sub>T<sub>x</sub> sheets can be easily controlled by changing the oxidation duration, which is consistent with previous reports.<sup>[49]</sup> After the removal of TiO<sub>2</sub>, the Ti 2p spectra (Ti 2p<sub>3/2</sub> and Ti 2p<sub>1/2</sub>) can be fitted to several pairs of asymmetric peaks, corresponding to the interactions between Ti and C as well as other terminal atoms in Ti<sub>3</sub>C<sub>2</sub>T<sub>x</sub> (Figure 3c). With the increase of the oxidation time, C–Ti–O and C–Ti–OH ratio gradually increases from 9.92 at% in pristine Ti<sub>3</sub>C<sub>2</sub>T<sub>x</sub> to 15.01 at% in H-Ti<sub>3</sub>C<sub>2</sub>T<sub>x</sub>-40 (Table S2, Supporting Information).

The Raman spectra further show the structure and composition changes of Ti<sub>3</sub>C<sub>2</sub>T<sub>x</sub> at different oxidation time and etching process (Figure 3d). The vibration bands at 195 and 717 cm<sup>-1</sup> correspond to the typical A<sub>1g</sub> symmetry out-plane vibrations of Ti and C atoms. The bands at 288, 390, and 623 cm<sup>-1</sup> are ascribed to be the in-plane vibration of the E<sub>g</sub> group of Ti, C, and surface functional groups.<sup>[51–53]</sup> For the O-Ti<sub>3</sub>C<sub>2</sub>T<sub>x</sub> films, the additional characteristic vibration band for anatase TiO<sub>2</sub> at 150 cm<sup>-1</sup> can be observed clearly.<sup>[54]</sup> The intensity of the band increases with the increment of the oxidization time, further confirms the formation of TiO<sub>2</sub> on Ti<sub>3</sub>C<sub>2</sub>T<sub>x</sub> sheets. After etching with HF solution, they disappear completely in the H-Ti<sub>3</sub>C<sub>2</sub>T<sub>x</sub> films. Besides these characteristic bands of Ti<sub>3</sub>C<sub>2</sub>T<sub>x</sub> in the range of 100–800 cm<sup>-1</sup>, two additional bands at 1347 and 1570 cm<sup>-1</sup> are observed for O-Ti<sub>3</sub>C<sub>2</sub>T<sub>x</sub> and H-Ti<sub>3</sub>C<sub>2</sub>T<sub>x</sub> products, which can be attributed to the carbon species (Figure 3e), and further proves the formation of carbon after the selective oxidation process.<sup>[44]</sup> The above results clearly demonstrate that both the chemical components and the surface chemistry of Ti<sub>3</sub>C<sub>2</sub>T<sub>x</sub> nanosheets can be precisely manipulated by the controllable oxidation and etching process.

By vacuum filtration of the pristine Ti<sub>3</sub>C<sub>2</sub>T<sub>x</sub> and H-Ti<sub>3</sub>C<sub>2</sub>T<sub>x</sub> dispersion, it is ready to assemble these H-Ti<sub>3</sub>C<sub>2</sub>T<sub>x</sub> nanosheets to self-standing films (Figure 4a). From the top-view SEM images, considerable wrinkles can be found on the surface of both pristine Ti<sub>3</sub>C<sub>2</sub>T<sub>x</sub> and H-Ti<sub>3</sub>C<sub>2</sub>T<sub>x</sub> film (Figure 4b,c). Besides, the surface of H-Ti<sub>3</sub>C<sub>2</sub>T<sub>x</sub> films becomes rougher with the prolongation of oxidation time from 10 to 40 min (Figure 4c–e). Such phenomenon is probably caused by the overlapping fragments arising from the reduced lateral size of the nanosheets, which is considered to be caused by the oxidation process. Under the same film thickness of 25 μm, four-probe measurement reveals that electrical conductivities of H-Ti<sub>3</sub>C<sub>2</sub>T<sub>x</sub>-10, H-Ti<sub>3</sub>C<sub>2</sub>T<sub>x</sub>-25, and H-Ti<sub>3</sub>C<sub>2</sub>T<sub>x</sub>-40 film are 1388, 889, and 201 S cm<sup>-1</sup>, respectively, which is consistent with the higher defect and hole density on Ti<sub>3</sub>C<sub>2</sub>T<sub>x</sub> sheets after long time hydrothermal oxidation.<sup>[49]</sup> Figure S7, Supporting Information, provides the side-view SEM images of the pristine Ti<sub>3</sub>C<sub>2</sub>T<sub>x</sub> and H-Ti<sub>3</sub>C<sub>2</sub>T<sub>x</sub>-40 film. The H-Ti<sub>3</sub>C<sub>2</sub>T<sub>x</sub>-40 film exhibits more messy and fluffy film structure, which is considered to promote the

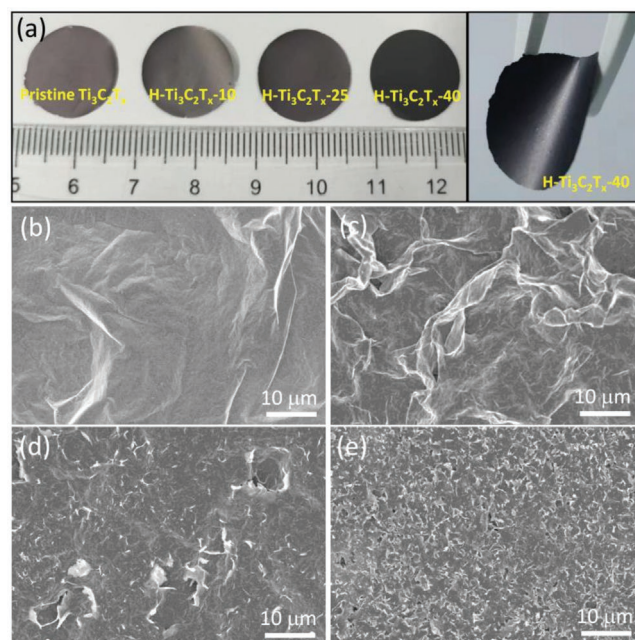


**Figure 4.** Optical photographs and SEM characterization results: a) optical photos of pristine Ti<sub>3</sub>C<sub>2</sub>T<sub>x</sub> and H-Ti<sub>3</sub>C<sub>2</sub>T<sub>x</sub> films, b) top-view SEM images of pristine Ti<sub>3</sub>C<sub>2</sub>T<sub>x</sub> film, c) H-Ti<sub>3</sub>C<sub>2</sub>T<sub>x</sub>-10 film, d) H-Ti<sub>3</sub>C<sub>2</sub>T<sub>x</sub>-25 film, and e) H-Ti<sub>3</sub>C<sub>2</sub>T<sub>x</sub>-40 film.

ion transport by providing more shortcuts perpendicular to the restacked film.<sup>[46]</sup>

The electrochemical performances of the H-Ti<sub>3</sub>C<sub>2</sub>T<sub>x</sub> films were evaluated in a three-electrode system by using 3 M H<sub>2</sub>SO<sub>4</sub> aqueous solution as the electrolyte and activated carbon as the counter electrode. The CV curves at 3 mV s<sup>-1</sup> of the pristine Ti<sub>3</sub>C<sub>2</sub>T<sub>x</sub> and the H-Ti<sub>3</sub>C<sub>2</sub>T<sub>x</sub> films with the same thickness of 25 μm are compared in Figure 5a. For each electrode, a pair of redox peaks on a rectangle shaped curve can be observed for the Ti<sub>3</sub>C<sub>2</sub>T<sub>x</sub>-based electrodes, suggesting the combination of pseudocapacitive nature and the double-layer capacitance.<sup>[55,56]</sup> Moreover, the H-Ti<sub>3</sub>C<sub>2</sub>T<sub>x</sub> electrodes show much enhanced current response and significantly increased integrated area than the pristine Ti<sub>3</sub>C<sub>2</sub>T<sub>x</sub> electrode. This observation suggests that those in-plane nanopores in H-Ti<sub>3</sub>C<sub>2</sub>T<sub>x</sub> sheets contribute more exposed electroactive sites. The specific capacitances of H-Ti<sub>3</sub>C<sub>2</sub>T<sub>x</sub> electrodes with the thickness of 25 μm at the current densities ranging from 0.5 to 50 A g<sup>-1</sup> are plotted in Figure 5b. It is noticed that the gravimetric capacitance enhances gradually with the oxidation time and the maximal value of 339 F g<sup>-1</sup> is achieved for H-Ti<sub>3</sub>C<sub>2</sub>T<sub>x</sub>-40 at 0.5 A g<sup>-1</sup>. Such value can retain as high as 196 F g<sup>-1</sup> even at high current density of 50 A g<sup>-1</sup>. Obviously, the performance of H-Ti<sub>3</sub>C<sub>2</sub>T<sub>x</sub>-40 is much superior to that of pristine Ti<sub>3</sub>C<sub>2</sub>T<sub>x</sub> which only has the specific capacity of 258 F g<sup>-1</sup> at 0.5 A g<sup>-1</sup> and rapidly drops to 20 F g<sup>-1</sup> at 50 A g<sup>-1</sup>. Such comparison clearly reveals that those in-plane nanopores not only enhance the specific capacitance but also remarkably facilitate the ion transport in the film electrodes. The ion transport properties within the electrodes are also evaluated by electrochemical impedance spectroscopy (EIS) (Figure 5c). Compared to the pristine Ti<sub>3</sub>C<sub>2</sub>T<sub>x</sub> electrode, the Nyquist plots of H-Ti<sub>3</sub>C<sub>2</sub>T<sub>x</sub> electrodes are almost perpendicular to the real axis

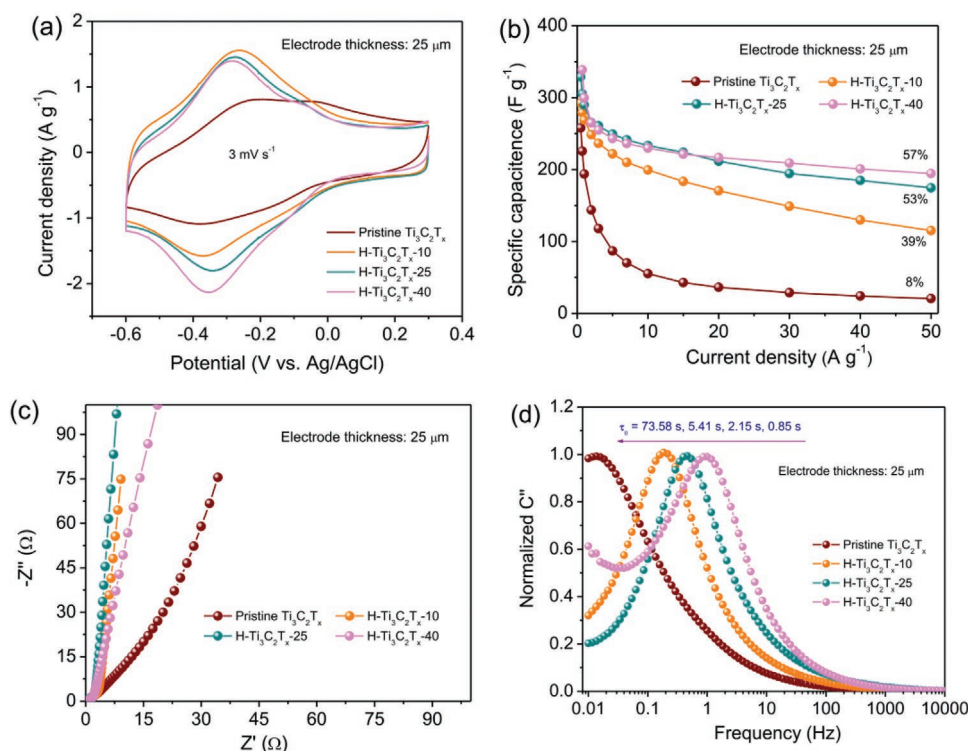


**Figure 5.** Electrochemical properties of H-Ti<sub>3</sub>C<sub>2</sub>T<sub>x</sub> electrodes with film thickness of 25 μm in 3 M H<sub>2</sub>SO<sub>4</sub> electrolyte: a) CV curves at 3 mV s<sup>-1</sup>, b) specific capacitances and retentions in 0.5–50 A g<sup>-1</sup>, c) Nyquist plots, and d) relaxation time constants derived from the normalized imaginary part capacitance.

in the whole-frequency range, confirming an ideal capacitive behavior and fast ion transport kinetics.<sup>[46,57]</sup> Furthermore, the relaxation time constant ( $\tau_0$ ), which refers to the minimum time required to discharge all the energy with an efficiency of >50%, can be derived from the dependence of the imaginary ( $C''$ ) part on the frequency.<sup>[58]</sup> As shown in Figure S8, Supporting Information, the  $\tau_0$  of pristine Ti<sub>3</sub>C<sub>2</sub>T<sub>x</sub> film is 0.46, 2.0, and 73.58 s when film thickness is 5, 10, and 25 μm, respectively. The significantly large  $\tau_0$  at thicker film of 25 μm is obviously ascribed to the serious sheets stacking which hinders the ion access to the film interior. In contrast, the  $\tau_0$  of Ti<sub>3</sub>C<sub>2</sub>T<sub>x</sub>-10 dramatically decreases to 5.41 s and it continuously decreases to 2.15 and 0.85 for Ti<sub>3</sub>C<sub>2</sub>T<sub>x</sub>-25 and Ti<sub>3</sub>C<sub>2</sub>T<sub>x</sub>-40 film, respectively (Figure 5d). It is noted that the current response of H-Ti<sub>3</sub>C<sub>2</sub>T<sub>x</sub>-40 is almost 89 times faster than that of pristine Ti<sub>3</sub>C<sub>2</sub>T<sub>x</sub> electrode under the same film thickness of 25 μm. These results are in good agreement with the rate capability shown in Figure 5b, which demonstrates the significantly enhanced ion transport kinetics for H-Ti<sub>3</sub>C<sub>2</sub>T<sub>x</sub> electrodes.

According to the SEM images in Figure 4, the oxidation of Ti<sub>3</sub>C<sub>2</sub>T<sub>x</sub> sheets leads to the decrease of lateral size of Ti<sub>3</sub>C<sub>2</sub>T<sub>x</sub> nanosheets. In order to elucidate the size effects of Ti<sub>3</sub>C<sub>2</sub>T<sub>x</sub> sheets on their ion transport kinetics, the pristine Ti<sub>3</sub>C<sub>2</sub>T<sub>x</sub> has been sonicated at 230 W for 2 and 3 h, which yields Ti<sub>3</sub>C<sub>2</sub>T<sub>x</sub> with average hydrodynamic size of around 280 and 240 nm, respectively (Figure S9, Supporting Information). Their capacitive performance has been tested and compared with the H-Ti<sub>3</sub>C<sub>2</sub>T<sub>x</sub>-25 electrode at the same film thickness of 10 μm. Figure 6a shows the CV curves of pristine Ti<sub>3</sub>C<sub>2</sub>T<sub>x</sub>, sonicated Ti<sub>3</sub>C<sub>2</sub>T<sub>x</sub> and the H-Ti<sub>3</sub>C<sub>2</sub>T<sub>x</sub>-25 film. All the films present similar

shape, while the sonicated Ti<sub>3</sub>C<sub>2</sub>T<sub>x</sub> films show slightly larger integrated area when compared with that of pristine Ti<sub>3</sub>C<sub>2</sub>T<sub>x</sub>, which agrees well with previous reported results.<sup>[59]</sup> The specific capacitance of these samples under the scan rate range of 10–3000 mV s<sup>-1</sup> is illustrated in Figure 6b. The Ti<sub>3</sub>C<sub>2</sub>T<sub>x</sub> film sonicated for 2 h remains roughly similar property with the pristine film. Although the Ti<sub>3</sub>C<sub>2</sub>T<sub>x</sub> film sonicated for 3 h displays enhanced property, its performance is still much lower than that of the H-Ti<sub>3</sub>C<sub>2</sub>T<sub>x</sub>-25 electrode. The comparison of the relaxation time constant in Figure 6c also clearly demonstrates that the smallest  $\tau_0$  of 1.00 s is achieved for H-Ti<sub>3</sub>C<sub>2</sub>T<sub>x</sub>-25 sample, which is much smaller than those of the sonicated or the pristine Ti<sub>3</sub>C<sub>2</sub>T<sub>x</sub> samples. Considering that the average hydrodynamic diameter of the sonicated Ti<sub>3</sub>C<sub>2</sub>T<sub>x</sub> is comparable to the lateral size of the H-Ti<sub>3</sub>C<sub>2</sub>T<sub>x</sub>-25 and H-Ti<sub>3</sub>C<sub>2</sub>T<sub>x</sub>-40 (Figure 1f,g), the above results demonstrate that the dramatically enhanced ion kinetics of H-Ti<sub>3</sub>C<sub>2</sub>T<sub>x</sub>-25 is mainly originated from the in-plane nanopores instead of the reduced size effect.

Taking H-Ti<sub>3</sub>C<sub>2</sub>T<sub>x</sub>-25 as an example, we further study the dependence of specific capacitance on the electrode thickness. In this case, the H-Ti<sub>3</sub>C<sub>2</sub>T<sub>x</sub>-25 films with thicknesses varying from 10 to 84 μm have been investigated accordingly. The thickness changes correspond to a mass loading increase from 1.63 to 6.41 mg cm<sup>-2</sup> (Figure 6d). Figure S10, Supporting Information, shows the typical GCD curves of H-Ti<sub>3</sub>C<sub>2</sub>T<sub>x</sub>-25 electrode with different film thicknesses under the current density range from 1 to 10 A g<sup>-1</sup>. Regardless of the film thickness, all the GCD curves keep nearly symmetric features with conspicuous voltage plateaus ranging from -0.35 to -0.45 V, confirming the highly reversible electrochemical

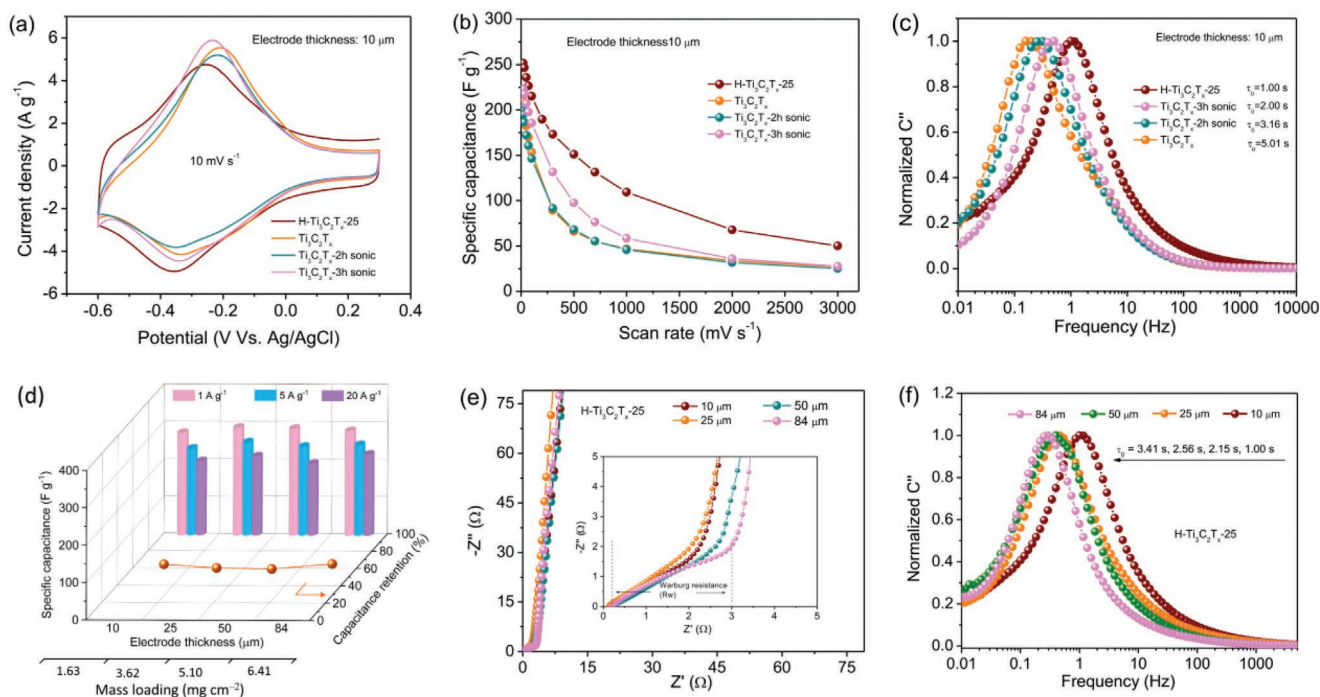


**Figure 6.** a–c) Performance comparison of H-Ti<sub>3</sub>C<sub>2</sub>T<sub>x</sub>-25 film with pristine Ti<sub>3</sub>C<sub>2</sub>T<sub>x</sub> and sonicated Ti<sub>3</sub>C<sub>2</sub>T<sub>x</sub> for 2 and 3 h: a) CV curves at 10 mV s<sup>-1</sup>, b) rate capability in 10–3000 mV s<sup>-1</sup>, and c) relaxation time constant. d,e) Electrochemical performance of H-Ti<sub>3</sub>C<sub>2</sub>T<sub>x</sub>-25 films of different thicknesses: d) specific capacitances at 0.5, 5.0, and 20 A g<sup>-1</sup> and capacitance retention in the range of 0.5–50 A g<sup>-1</sup> and e) Nyquist plots with inset showing the Warburg resistance. f) Relaxation time constants derived from the normalized imaginary part capacitance.

reactions proceeding between the electrodes and electrolyte. An interesting result is that even though the electrode thickness increases from 10 to 25, 50, and 84 μm, the specific capacitances of H-Ti<sub>3</sub>C<sub>2</sub>T<sub>x</sub>-25 electrodes remain at 274, 288, 286, and 280 F g<sup>-1</sup> at 1.0 A g<sup>-1</sup>, respectively (Figure 6d and Figure S10e, Supporting Information). Considering the corresponding mass loadings, their volumetric capacitances are calculated to be 446, 419, 291, and 214 F cm<sup>-3</sup> at 10, 25, 50, and 84 μm, respectively. When the current density increases to 5 and 20 A g<sup>-1</sup>, the specific capacitance of H-Ti<sub>3</sub>C<sub>2</sub>T<sub>x</sub>-25 electrode also presents thickness-independent performances (Figure 6d and Figure S10a–d, Supporting Information). Moreover, the H-Ti<sub>3</sub>C<sub>2</sub>T<sub>x</sub>-25 electrode is capable of maintaining around 60% capacitance as the current density increases by 50 times (1–50 A g<sup>-1</sup>) (Figure 6a and Figure S11, Supporting Information). It is noted that H-Ti<sub>3</sub>C<sub>2</sub>T<sub>x</sub> prepared in this work is comparable or even better than the previous reported holey Ti<sub>3</sub>C<sub>2</sub>T<sub>x</sub> in term of specific capacitance and rate capability. Moreover, the performance of the reported holey Ti<sub>3</sub>C<sub>2</sub>T<sub>x</sub> in the references is usually achieved under very thin film thickness or low mass loading (Table S4, Supporting Information). The thickness-independent electrochemical properties achieved by the H-Ti<sub>3</sub>C<sub>2</sub>T<sub>x</sub>-25 electrode verify the crucial role of in-plane nanopores in boosting the ion penetration. The fast ion transport kinetics in H-Ti<sub>3</sub>C<sub>2</sub>T<sub>x</sub>-25 electrodes are also reflected in their Nyquist plots. In Figure 6e, the solution resistance and charge transfer resistance keep nearly unchanged for the same H-Ti<sub>3</sub>C<sub>2</sub>T<sub>x</sub>-25 electrodes because they have almost the same electrical conductivity and are tested in the same electrolyte. In this way, the change of the ion diffusion resistance can be evaluated by the difference in Warburg resistance (inset in

Figure 6e). Despite the notable increase of the electrode thickness from 10 to 84 μm, the Warburg resistance only increases from 1.91 to 2.84 ohm (Table S3, Supporting Information), suggesting a fast ion transport in this thicker film. The relaxation time constants of the H-Ti<sub>3</sub>C<sub>2</sub>T<sub>x</sub>-25 electrodes with different film thicknesses also support this conclusion. As shown in Figure 6f, the τ<sub>0</sub> is determined to be 1.00, 2.15, 2.56, and 3.41 s with electrode thickness of 10, 25, 50, and 84 μm, respectively. Our findings show that τ<sub>0</sub> does not change significantly with the electrode thickness, implying that the ion diffusion kinetics are hardly affected by the thicker electrode. It is also noted that small τ<sub>0</sub> achieved by the H-Ti<sub>3</sub>C<sub>2</sub>T<sub>x</sub>-25 film is much superior to those of pure Ti<sub>3</sub>C<sub>2</sub>T<sub>x</sub> film (4.4 s),<sup>[58]</sup> dry Ti<sub>3</sub>C<sub>2</sub>T<sub>x</sub> Film (1.49 s),<sup>[60]</sup> Ti<sub>3</sub>C<sub>2</sub> film (6.8 s), diethanolamine-Ti<sub>3</sub>C<sub>2</sub>T<sub>x</sub> (4.6 s),<sup>[61]</sup> and MXene-rGO films (1.75 s).<sup>[62]</sup>

To further elucidate the fast ion transport kinetics in thick H-Ti<sub>3</sub>C<sub>2</sub>T<sub>x</sub>-25 film, the capacitive performance of the film with the thickness increased up to 84 μm has been investigated. The CV profiles of this film at low scan rate of 3–500 mV s<sup>-1</sup> is provided in Figure S12, Supporting Information, and Figure 7a. From these figures, the linear increase of the current under different scan rate reveals the excellent rate capability and reversibility of the electrodes. Even increasing the high scan rate up to 20 V s<sup>-1</sup>, the shape of CV curves does not deform significantly (Figure 7b). In order to further elucidate this high-rate capability, log(current/mA) versus log(scan rate/mV s<sup>-1</sup>) following the equation  $i = av^b$  have been plotted in Figure 7c. In this equation,  $v$  is the scan rate,  $i$  is the peak current at different scan rates, and  $a$  and  $b$  are adjustable values.<sup>[63,64]</sup> In general,  $b = 0.5$  suggests the diffusion-controlled electrochemical

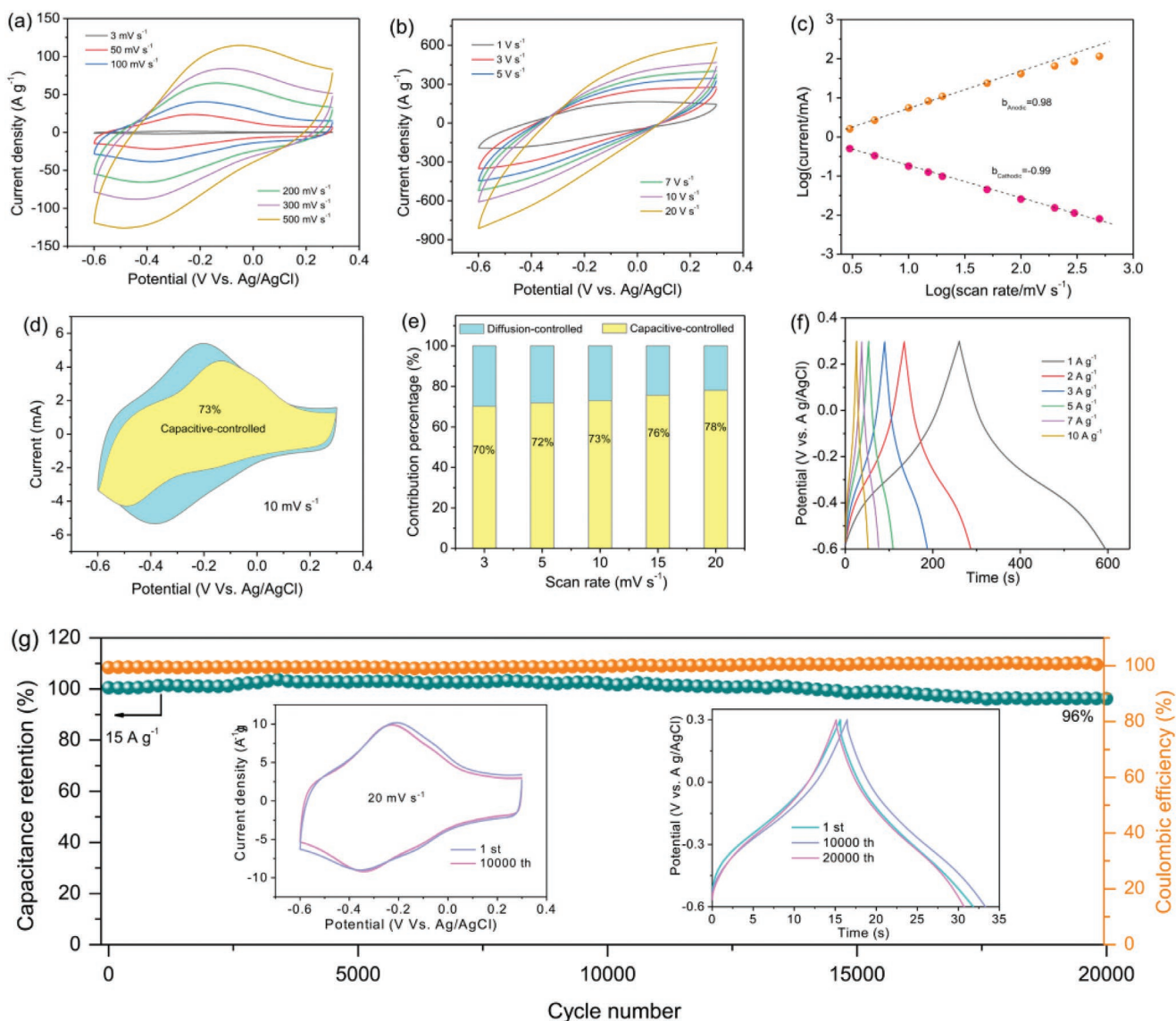


**Figure 7.** Electrochemical performance of the H-Ti<sub>3</sub>C<sub>2</sub>T<sub>x</sub>-25 electrode with 84  $\mu\text{m}$  thickness. a,b) CV curves at low and high scan rates, c) plots of  $\log(i)$  versus  $\log(v)$  in the scan rates range from 3 to 500  $\text{mV s}^{-1}$ , d) CV response at a scan rate of 5  $\text{mV s}^{-1}$  with the yellow shaded area corresponding to the capacitive contribution, e) percentage of capacitive contribution in the total capacitance at diverse scan rates, f) GCD curves at different current densities, and g) cycling performance at 15  $\text{A g}^{-1}$  with inset showing the CV and GCD curves recorded at different cycling stages.

process, while  $b = 1$  indicates a capacitive-controlled process. By linear fitting of the plots under the scan rate range of 3–500  $\text{mV s}^{-1}$ , the  $b$  values are 0.98 and 0.99 for anodic and cathodic peaks, respectively. The results in Figure 7c reveal that H-Ti<sub>3</sub>C<sub>2</sub>T<sub>x</sub>-25 film exhibits the fast capacitive energy storage behavior, where the electrolyte ions can rapidly penetrate the dense film through these in-plane pores even with the film thickness of 84  $\mu\text{m}$ .

To distinguish quantitatively the capacitive contribution, we applied the Dunn's method to analyze the current:

$$i(V) = k_1v + k_2v^{1/2} \quad (1)$$

$$i(V)/v^{1/2} = k_1v^{1/2} + k_2 \quad (2)$$

where  $k_1v$  and  $k_2v^{1/2}$  correspond to the current contributions from the surface capacitive and the diffusion-controlled process, respectively.<sup>[65,66]</sup> The CV curve for the H-Ti<sub>3</sub>C<sub>2</sub>T<sub>x</sub>-25 electrode is presented in Figure 7d, in which the shaded area corresponds to the current contribution from the capacitive controlled process. It is noticed that about 70% current is contributed from the capacitive process at low scan rate of 3  $\text{mV s}^{-1}$ . This capacitive contribution increases gradually with the scan rate and reaches 78% at 20  $\text{mV s}^{-1}$  (Figure 7e). The above observations confirm that the storage of H<sup>+</sup> in H-Ti<sub>3</sub>C<sub>2</sub>T<sub>x</sub>-25 is achieved by a fast capacitive process. In addition, the GCD profiles at different current densities also show good symmetry (Figure 7f), which means the reversible H<sup>+</sup> storage in this thick film electrode. The long-term cycling performance of the H-Ti<sub>3</sub>C<sub>2</sub>T<sub>x</sub>-25 electrode was also investigated at the current density of 15  $\text{A g}^{-1}$ .

The H-Ti<sub>3</sub>C<sub>2</sub>T<sub>x</sub>-25 film retains 96% of its initial capacitance and exhibits an excellent Coulombic efficiency of ≈100% after 20 000 galvanostatic charge–discharge cycles (Figure 7g). The CV and GCD profiles before and after cycles display negligible change (inset in Figure 7g), confirming an ultra-stable cycling performance of H-Ti<sub>3</sub>C<sub>2</sub>T<sub>x</sub> electrodes.

### 3. Conclusions

In summary, we have developed a mild oxidation route to prepare holey Ti<sub>3</sub>C<sub>2</sub>T<sub>x</sub> nanosheets by introducing O<sub>2</sub> during refluxing of the pristine MXene suspension at 100 °C. The H-Ti<sub>3</sub>C<sub>2</sub>T<sub>x</sub> obtained at longer oxidation time exhibits larger specific capacitance together with higher rate capability and rapid current response, which can be attributed to the rich defect states and pore structures at the surface. Electrochemical characterizations reveal that these H-Ti<sub>3</sub>C<sub>2</sub>T<sub>x</sub> films demonstrate nearly thickness-independence capacitive properties with specific capacitance of 320 F g<sup>-1</sup> (476 F cm<sup>-3</sup>) at thickness of 10 μm (1.63 mg cm<sup>-2</sup>), which maintains 323 F g<sup>-1</sup> (246 F cm<sup>-3</sup>) as the film thickness increase to 84 μm (6.41 mg cm<sup>-2</sup>). The EIS reveals that the relaxation time constants of H-Ti<sub>3</sub>C<sub>2</sub>T<sub>x</sub>-25 electrode are also less dependent on the film thickness. Such extraordinary properties demonstrate that these in-plane nanopores not only contribute to a high specific capacitance but also offer numerous pathways for rapid penetration of electrolyte ions across the dense film electrode. Our findings may offer a new avenue to circumvent the sheet restacking that would impede ion transport within the dense MXene film.

### 4. Experimental Section

**Materials Preparation:** The Ti<sub>3</sub>C<sub>2</sub>T<sub>x</sub> was prepared by etching Ti<sub>3</sub>AlC<sub>2</sub> with a mixture of LiF and HCl to selectively remove Al layers following a method reported previously.<sup>[47]</sup> Specifically, 3.2 g of LiF was slowly added into 60 mL of 9 M HCl under stirring. Then, 2 g Ti<sub>3</sub>AlC<sub>2</sub> powder (purchased from 11 Technology Co. Ltd.) were slowly added to the above solution and continuously stirred at 35 °C for 24 h. The acquired resultant was repeatedly centrifuged with ultrapure water at 4 °C until the pH of the supernatant reached 7.0. Afterward, the swollen Ti<sub>3</sub>C<sub>2</sub>T<sub>x</sub> slurry was separated from the mixture by centrifugation at 3500 rpm for 2 min. Finally, the delaminated Ti<sub>3</sub>C<sub>2</sub>T<sub>x</sub> colloidal dispersion could be obtained after ultrasonication for 1 h under the protection of bubbling Ar gas.

The oxidation of the Ti<sub>3</sub>C<sub>2</sub>T<sub>x</sub> nanosheets was performed by adding 20 mL of Ti<sub>3</sub>C<sub>2</sub>T<sub>x</sub> colloidal dispersion (1.9 mg mL<sup>-1</sup>) in a 100 mL three-necked flask equipped with a high purity oxygen inlet/outlet and spherical condenser tube for condensate reflux. As the temperature of the dispersion raised at 100 °C, high purity oxygen was injected at a rate of 200 SCCM to allow it to bubble below the surface of the dispersion for 10, 25, and 40 min. The oxidized Ti<sub>3</sub>C<sub>2</sub>T<sub>x</sub> was denoted as O-Ti<sub>3</sub>C<sub>2</sub>T<sub>x</sub>-x with x representing the oxidation duration in minutes. Finally, the O-Ti<sub>3</sub>C<sub>2</sub>T<sub>x</sub>-x was dispersed in 20 mL of 10% v/v HF acid solution at room temperature for 6 h to etch away the obtained TiO<sub>2</sub>, leaving behind in-plane nanopores in Ti<sub>3</sub>C<sub>2</sub>T<sub>x</sub> sheets which referred to holey Ti<sub>3</sub>C<sub>2</sub>T<sub>x</sub> (H-Ti<sub>3</sub>C<sub>2</sub>T<sub>x</sub>). The O-Ti<sub>3</sub>C<sub>2</sub>T<sub>x</sub> and H-Ti<sub>3</sub>C<sub>2</sub>T<sub>x</sub> film were obtained by filtering corresponding dispersion on a PVDF filter membrane (100 nm pore size) using vacuum-assisted filtration and the film thickness could be facilely tuned using various amounts of dispersions.

**Materials Characterization:** The morphology of the samples was characterized by a field-emission scanning electron

microscope (SU8020) and a TEM (JEM-2800). The phase structure of the products was identified on a DX-2700 X-ray diffractometer with Cu K<sub>α</sub> radiation (λ = 0.154 nm, 40 kV). The XPS spectra were collected on an ESCALAB Xi+ X-ray photoelectron spectrometer (Thermo Fisher Scientific) using a monochromatized Al K<sub>α</sub> X-ray source (1486.8 eV). The binding energy was corrected by the C 1s line at 284.8 eV. Raman spectra were collected on a Renishaw inVia Raman microscope with an excitation wavelength of 532 nm.

**Electrochemical Measurements:** All electrochemical experiments were carried out on Gamary electrochemical workstation within the operation potential between -0.6 and 0.3 V (vs Ag/AgCl) in a plastic three-electrode Swagelok setup, where the Ti<sub>3</sub>C<sub>2</sub>T<sub>x</sub> film served as working electrodes, activated carbon as the counter electrode, and Ag/AgCl as the reference electrode. The counter electrode was prepared by mechanically mixing YP-50, carbon black, and PTFE binder in a mass ratio of 87:10:3 in ethanol. After evaporation of solvent in the slurry, the mixture was rolled into a thick sheet and punched into a circular disk with diameter of 5 mm. The Celgard 3501 membrane was used as separators and 3 M aqueous H<sub>2</sub>SO<sub>4</sub> was used as electrolytes. EIS was tested at a frequency range varying from 0.001 to 100 kHz with an amplitude of 5 mV. The gravimetric specific capacitance was calculated based on the GCD curves according to the following formulas:<sup>[67,68]</sup>

$$C = \frac{2I \int V dt}{mV^2 |V_i} \quad (3)$$

where  $I$  was the discharge current (A),  $m$  was the mass of the Ti<sub>3</sub>C<sub>2</sub>T<sub>x</sub> electrode (g),  $\int V dt$  was the integral current area of the discharge curve, and  $V$  was the potential window varying from initial  $V_i$  to final value  $V_f$ . The real  $C'(\omega)$  and imaginary part  $C''(\omega)$  capacitances were derived from the following formulas:<sup>[69]</sup>

$$C'(\omega) = \frac{-Z''(\omega)}{\omega |Z(\omega)|^2} \quad (4)$$

$$C''(\omega) = \frac{Z'(\omega)}{\omega |Z(\omega)|^2} \quad (5)$$

where  $\omega$  was the angular frequency ( $\omega = 2\pi f$ ),  $f$  was frequency (Hz),  $Z'(\omega)$  and  $Z''(\omega)$  were real and imaginary parts of  $Z(\omega)$ , respectively.

**Statistical Analysis:** Pore size of H-Ti<sub>3</sub>C<sub>2</sub>T<sub>x</sub> sheets was statistically analyzed using Nano Measure software based on the TEM images. About 70 pores for H-Ti<sub>3</sub>C<sub>2</sub>T<sub>x</sub>-10, 220 pores for H-Ti<sub>3</sub>C<sub>2</sub>T<sub>x</sub>-25, and 440 pores for H-Ti<sub>3</sub>C<sub>2</sub>T<sub>x</sub>-40 were counted for size analysis.

### Supporting Information

Supporting Information is available from the Wiley Online Library or from the author.

### Acknowledgements

This work was supported by the National Natural Science Foundation of China (No. 51772181), the Natural Science Basic Research Plan of Shaanxi Province (No. 2019JLP-12), and Shaanxi Sanqin Scholars Innovation Team. R.G. is also grateful for the fellowship from the China Scholarship Council (202106870046).

### Conflict of Interest

The authors declare no conflict of interest.

## Data Availability Statement

The data that support the findings of this study are available from the corresponding author upon reasonable request.

## Keywords

capacitive performances, controllable oxidation, holey  $\text{Ti}_3\text{C}_2\text{T}_x$ , supercapacitors, thick film electrodes

Received: September 27, 2022

Revised: December 5, 2022

Published online:

- [1] J. Zhao, A. F. Burke, *Adv. Energy Mater.* **2020**, *11*, 2002192.
- [2] P. Simon, Y. Gogotsi, B. Dunn, *Science* **2014**, *343*, 1210.
- [3] J. R. Miller, P. Simon, *Science* **2008**, *321*, 651.
- [4] Y. Zhou, H. Qi, J. Yang, Z. Bo, F. Huang, M. S. Islam, X. Lu, L. Dai, R. Amal, C. H. Wang, Z. Han, *Energy Environ. Sci.* **2021**, *14*, 1854.
- [5] P. Xie, W. Yuan, X. Liu, Y. Peng, Y. Yin, Y. Li, Z. Wu, *Energy Storage Mater.* **2021**, *36*, 56.
- [6] W. Guo, C. Yu, S. Li, J. Qiu, *Energy Environ. Sci.* **2021**, *14*, 576.
- [7] Y. Gao, C. Xie, Z. Zheng, *Adv. Energy Mater.* **2020**, *11*, 2002838.
- [8] Y. Gogotsi, R. M. Penner, *ACS Nano* **2018**, *12*, 2081.
- [9] J. Chen, P. S. Lee, *Adv. Energy Mater.* **2020**, *11*, 2003311.
- [10] Z. Lei, J. Zhang, L. L. Zhang, N. A. Kumar, X. S. Zhao, *Energy Environ. Sci.* **2016**, *9*, 1891.
- [11] Z. Yang, J. Tian, Z. Yin, C. Cui, W. Qian, F. Wei, *Carbon* **2019**, *141*, 467.
- [12] M. Athanasiou, S. N. Yannopoulos, T. Ioannides, *Chem. Eng. J.* **2022**, *446*, 137191.
- [13] J. Wang, X. Zhang, Z. Li, Y. Ma, L. Ma, *J. Power Sources* **2020**, *451*, 227794.
- [14] Q. Z. Zhang, D. Zhang, Z. C. Miao, X. L. Zhang, S. L. Chou, *Small* **2018**, *14*, 1702883.
- [15] T. Li, W. Zhang, L. Zhi, H. Yu, L. Dang, F. Shi, H. Xu, F. Hu, Z. Liu, Z. Lei, J. Qiu, *Nano Energy* **2016**, *30*, 9.
- [16] H. Li, S. Lin, H. Li, Z. Wu, Q. Chen, L. Zhu, C. Li, X. Zhu, Y. Sun, *Small Methods* **2022**, *6*, 2101320.
- [17] H. Kuang, H. Zhang, X. Liu, Y. Chen, W. Zhang, H. Chen, Q. Ling, *Carbon* **2022**, *190*, 57.
- [18] X. Xiong, D. Ding, D. Chen, G. Waller, Y. Bu, Z. Wang, M. Liu, *Nano Energy* **2015**, *11*, 154.
- [19] X. Li, Z. Huang, C. E. Shuck, G. Liang, Y. Gogotsi, C. Zhi, *Nat. Rev. Chem.* **2022**, *6*, 389.
- [20] X. Xu, Y. Zhang, H. Sun, J. Zhou, F. Yang, H. Li, H. Chen, Y. Chen, Z. Liu, Z. Qiu, D. Wang, L. Ma, J. Wang, Q. Zeng, Z. Peng, *Adv. Electron. Mater.* **2021**, *7*, 2000967.
- [21] D. Xiong, Y. Shi, H. Y. Yang, *Mater. Today* **2021**, *46*, 183.
- [22] Z. Li, N. H. Attanayake, J. L. Blackburn, E. M. Miller, *Energy Environ. Sci.* **2021**, *14*, 6242.
- [23] B. Wei, Z. Fu, D. Legut, T. C. Germann, S. Du, H. Zhang, J. S. Francisco, R. Zhang, *Adv. Mater.* **2021**, *33*, 2102595.
- [24] J. Yin, B. Ge, T. Jiao, Z. Qin, M. Yu, L. Zhang, Q. Zhang, Q. Peng, *Langmuir* **2021**, *37*, 1267.
- [25] K. Rasool, R. P. Pandey, P. A. Rasheed, S. Buczek, Y. Gogotsi, K. A. Mahmoud, *Mater. Today* **2019**, *30*, 80.
- [26] Y. Pei, X. Zhang, Z. Hui, J. Zhou, X. Huang, G. Sun, W. Huang, *ACS Nano* **2021**, *15*, 3996.
- [27] D. H. Ho, Y. Y. Choi, S. B. Jo, J. M. Myoung, J. H. Cho, *Adv. Mater.* **2021**, *33*, 2005846.
- [28] F. Damiri, M. H. Rahman, M. Zehravi, A. A. Awaji, M. Z. Nasrullah, H. A. Gad, M. Z. Bani-Fwaz, R. S. Varma, M. O. Germoush, H. S. Al-Malky, A. A. Sayed, S. Rojekar, M. M. Abdel-Daim, M. Berrada, *Materials* **2022**, *15*, 1666.
- [29] B. Lu, Z. Zhu, B. Ma, W. Wang, R. Zhu, J. Zhang, *Small* **2021**, *17*, 2100946.
- [30] A. VahidMohammadi, J. Rosen, Y. Gogotsi, *Science* **2021**, *372*, eabf1581.
- [31] Y. Wei, P. Zhang, R. A. Soomro, Q. Zhu, B. Xu, *Adv. Mater.* **2021**, *33*, 2103148.
- [32] M. Naguib, M. Kurtoglu, V. Presser, J. Lu, J. Niu, M. Heon, L. Hultman, Y. Gogotsi, M. W. Barsoum, *Adv. Mater.* **2011**, *23*, 4248.
- [33] M. K. Aslam, Y. Niu, M. Xu, *Adv. Energy Mater.* **2020**, *11*, 2000681.
- [34] J. Pang, R. G. Mendes, A. Bachmatyuk, L. Zhao, H. Q. Ta, T. Gemming, H. Liu, Z. Liu, M. H. Rummeli, *Chem. Soc. Rev.* **2019**, *48*, 72.
- [35] M. R. Lukatskaya, O. Mashtalir, C. E. Ren, Y. Dall'Agnese, P. Rozier, P. L. Taberna, M. Naguib, P. Simon, M. W. Barsoum, Y. Gogotsi, *Science* **2013**, *341*, 1502.
- [36] Y. Xia, T. S. Mathis, M. Q. Zhao, B. Anasori, A. Dang, Z. Zhou, H. Cho, Y. Gogotsi, S. Yang, *Nature* **2018**, *557*, 409.
- [37] T. Shang, Z. Lin, C. Qi, X. Liu, P. Li, Y. Tao, Z. Wu, D. Li, P. Simon, Q. H. Yang, *Adv. Funct. Mater.* **2019**, *29*, 1903960.
- [38] Y. Deng, T. Shang, Z. Wu, Y. Tao, C. Luo, J. Liang, D. Han, R. Lyu, C. Qi, W. Lv, F. Kang, Q. H. Yang, *Adv. Mater.* **2019**, *31*, 1902432.
- [39] E. Kim, B.-J. Lee, K. Maleski, Y. Chae, Y. Lee, Y. Gogotsi, C. W. Ahn, *Nano Energy* **2021**, *81*, 105616.
- [40] D. Wen, G. Ying, L. Liu, C. Sun, Y. Li, Y. Zhao, Z. Ji, Y. Wu, J. Zhang, J. Zhang, X. Wang, *Adv. Mater. Interfaces* **2021**, *8*, 2101453.
- [41] P. Zhang, Q. Zhu, R. A. Soomro, S. He, N. Sun, N. Qiao, B. Xu, *Adv. Funct. Mater.* **2020**, *30*, 2000922.
- [42] Z. Fan, Y. Wang, Z. Xie, D. Wang, Y. Yuan, H. Kang, B. Su, Z. Cheng, Y. Liu, *Adv. Sci.* **2018**, *5*, 1800750.
- [43] G. S. Gund, J. H. Park, R. Harpalsinh, M. Kota, J. H. Shin, T.-i. Kim, Y. Gogotsi, H. S. Park, *Joule* **2019**, *3*, 164.
- [44] C. E. Ren, M. Q. Zhao, T. Makaryan, J. Halim, M. Boota, S. Kota, B. Anasori, M. W. Barsoum, Y. Gogotsi, *ChemElectroChem* **2016**, *3*, 689.
- [45] J. Tang, T. S. Mathis, N. Kurra, A. Sarycheva, X. Xiao, M. N. Hedhili, Q. Jiang, H. N. Alshareef, B. Xu, F. Pan, Y. Gogotsi, *Angew. Chem., Int. Ed.* **2019**, *58*, 17849.
- [46] J. Tang, T. Mathis, X. Zhong, X. Xiao, H. Wang, M. Anayee, F. Pan, B. Xu, Y. Gogotsi, *Adv. Energy Mater.* **2020**, *11*, 2003025.
- [47] R. Guo, X. Han, P. Yuan, X. He, Q. Li, J. Sun, L. Dang, Z. Liu, Y. Zhang, Z. Lei, *Nano Res.* **2021**, *15*, 3254.
- [48] M. A. F. Shahzad, C. B. Hatter, B. Anasori, S. M. Hong, C. M. Koo, Y. Gogotsi, *Science* **2016**, *353*, 1137.
- [49] L. Jiao, C. Zhang, C. Geng, S. Wu, H. Li, W. Lv, Y. Tao, Z. Chen, G. Zhou, J. Li, G. Ling, Y. Wan, Q. H. Yang, *Adv. Energy Mater.* **2019**, *9*, 1900219.
- [50] X. Sang, Y. Xie, M.-W. Lin, M. Alhabeab, K. L. Van Aken, Y. Gogotsi, P. R. C. Kent, K. Xiao, R. R. Unocic, *ACS Nano* **2016**, *10*, 9193.
- [51] A. Sarycheva, T. Makaryan, K. Maleski, E. Satheeshkumar, A. Melikyan, H. Minassian, M. Yoshimura, Y. Gogotsi, *J. Phys. Chem. C* **2017**, *121*, 19983.
- [52] L. Zhang, W. Su, Y. Huang, H. Li, L. Fu, K. Song, X. Huang, J. Yu, C. T. Lin, *Nanoscale Res. Lett.* **2018**, *13*, 343.
- [53] A. Sarycheva, Y. Gogotsi, *Chem. Mater.* **2020**, *32*, 3480.
- [54] F. I. T. Ohsaka, Y. Fujiki, *J. Raman Spectrosc.* **1978**, *7*, 321.
- [55] X. Mu, D. Wang, F. Du, G. Chen, C. Wang, Y. Wei, Y. Gogotsi, Y. Gao, Y. Dall'Agnese, *Adv. Funct. Mater.* **2019**, *29*, 1902953.
- [56] Y. Ando, M. Okubo, A. Yamada, M. Otani, *Adv. Funct. Mater.* **2020**, *30*, 2000820.

- [57] T. S. M. J. Tang, N. Kurra, A. Sarycheva, X. Xiao, M. N. Hedhili, Q. Jiang, H. N. Alshareef, B. Xu, F. Pan, Y. Gogotsi, *Angew. Chem.* **2019**, *131*, 18013.
- [58] J. Yan, C. E. Ren, K. Maleski, C. B. Hatter, B. Anasori, P. Urbankowski, A. Sarycheva, Y. Gogotsi, *Adv. Funct. Mater.* **2017**, *27*, 1701264.
- [59] K. Maleski, C. E. Ren, M.-Q. Zhao, B. Anasori, Y. Gogotsi, *ACS Appl. Mater. Interfaces* **2018**, *10*, 24491.
- [60] J. Xu, X. Hu, X. Wang, X. Wang, Y. Ju, S. Ge, X. Lu, J. Ding, N. Yuan, Y. Gogotsi, *Energy Storage Mater.* **2020**, *33*, 382.
- [61] C. Yang, Y. Tang, C. Wei, W. Que, *J. Alloys Compd.* **2022**, *898*, 162882.
- [62] J. Miao, Q. Zhu, K. Li, P. Zhang, Q. Zhao, B. Xu, *J. Energy Chem.* **2021**, *52*, 243.
- [63] V. Augustyn, J. Come, M. A. Lowe, J. W. Kim, P. L. Taberna, S. H. Tolbert, H. D. Abruna, P. Simon, B. Dunn, *Nat. Mater.* **2013**, *12*, 518.
- [64] H. Lindström, S. Södergren, A. Solbrand, H. Rensmo, J. Hjelm, A. Hagfeldt, S.-E. Lindquist, *J. Phys. Chem. B* **1997**, *101*, 7717.
- [65] H. S. Kim, J. B. Cook, H. Lin, J. S. Ko, S. H. Tolbert, V. Ozolins, B. Dunn, *Nat. Mater.* **2017**, *16*, 454.
- [66] J. Wang, J. Polleux, J. Lim, B. Dunn, *J. Phys. Chem. C* **2007**, *111*, 14925.
- [67] R. Guo, J. Li, Y. Jia, F. Xin, J. Sun, L. Dang, Z. Liu, Z. Lei, *J. Mater. Chem. A* **2019**, *7*, 4165.
- [68] H. Sun, F. Niu, P. Yuan, X. He, J. Sun, Z. Liu, Q. Li, Z. Lei, *Small Struct.* **2021**, *2*, 2100029.
- [69] F. Niu, R. Guo, L. Dang, J. Sun, Q. Li, X. He, Z. Liu, Z. Lei, *ACS Appl. Energy Mater.* **2020**, *3*, 7794.